Supplementary Material

Selective persulfate activation over iron-alloy-based carbon aerogels

Min Chen[#], Yue Dou[#], Xu Liu, Yanchao Li, Hongying Zhao[*]

Shanghai Key Lab of Chemical Assessment and Sustainability, Key Laboratory of Yangtze River Water Environment, School of Chemical Science and Engineering, Tongji University, Shanghai 200092, China.
[#]These authors contributed equally to this work.

[*]**Correspondence to:** Prof. Hongying Zhao, Shanghai Key Lab of Chemical Assessment and Sustainability, Key Laboratory of Yangtze River Water Environment, School of Chemical Science and Engineering, Tongji University, Shanghai 200092, China. E-mail: hyzhao@tongji.edu.cn

Supplementary Texts

Supplementary Text 1. Chemicals and Reagents

Potassium peroxomonosulfate (PMS, $H_3K_5O_{18}S_4$, active oxygen > 4.5%), formaldehyde, resorcinol, iron acetylacetonate ($CHFeO_6$), molybdenum acetylacetonate ($C_{10}H_{14}MoO_6$), cobalt acetylacetonate ($CHCoO_4$), acetylacetone nickel ($CHNiO_4$), sodium carbonate (Na_2CO_3), ethanol (EtOH), naphthol, sodium thiosulfate (STS), methanol (MeOH), acetic acid (HAc), tert-butanol (TBA), furfuryl alcohol (FFA), benzoic acid (BA), sulfamethoxazole (SMX), tetracycline (TC), ciprofloxacin (CIP), nitrobenzene (NB), hydrochloric acid (HCl) sulfuric acid (H_2SO_4), sodium hydroxide (NaOH), sodium sulfate (Na_2SO_4), bisphenol-A (BPA), 5,5-dimethyl-1-pyrroline N-oxide (DMPO), 2,2,6,6-tetramethylpiperidine (TEMP), acetonitrile (HPLC grade) and methanol (HPLC grade) were purchased from Aladdin. All chemicals were of analytical grade and used as received without further purification.

Supplementary Text 2. Characterization Methods

Scanning electron microscopy (SEM) and transmission electron microscopy (TEM) images of as-prepared alloy-CA electrodes were obtained using a Hitachi S-4800 scanning electron microscope and a JEM-2010F electron microscope, respectively. The phases of alloy-CA were analyzed by X-ray diffraction (XRD; Rigaku D/max2550, Cu-Kα radiation, λ = 1.540562 Å, accelerating voltage 40 kV, current 40 mA, scanning range 10-80 °). Raman spectra of alloy-CA electrodes were recorded using a confocal Raman spectrometer (Renishaw, UK) with a 514 nm Ar^+ laser. *In situ* Raman experiments coupled with an electrochemical workstation were conducted to investigate the mechanism of PMS activation. X-ray photoelectron spectroscopy (XPS) was performed using a Thermo ESCALAB Xi^+ spectrometer with an Al Kα X-ray source under ultra-high vacuum conditions. The contents of metals in the catalysts and solutions were determined by inductively coupled plasma atomic emission spectroscopy (ICP-AES; 725-ES, Varian). The K-edge spectra of Fe, Co, Ni, and Mo were collected at the BL11B beamline of the Shanghai Synchrotron Radiation Facility (SSRF, Shanghai, China) using a Si(111) double-crystal monochromator. Prior to analysis, the samples were pressed into pellets 1 cm in diameter and sealed with polyimide tape. X-ray absorption fine structure (XAFS) spectra were recorded at room temperature using a four-channel silicon drift detector (SDD, Bruker 5040). The XAFS spectra of reference samples were collected in

fluorescence mode. Data processing and analysis were performed using the Athena and Artemis software packages, and wavelet transform analysis was conducted using the HAMA software.

Supplementary Text 3. Analytical procedures

The concentration of pollutants in reaction solution was analyzed by high-performance liquid chromatography (HPLC-UV, Agilent 1260II) with a reverse-phase ZORBAX Eclipse XDB-C18 column (5 μm particle size, 4.6 mm × 250 mm). The obtained testing samples were first collected and filtered through 0.22 μm PTFE filters. Then, the HPLC operating parameters were set as: methanol/water (65: 35, v/v) with 0.7 mL/min at λ = 225 nm for BPA, methanol/water (containing 1% acetic acid) (30: 70, v/v) with 0.8 mL/min at λ = 280 nm for SMX, methanol/water (containing 1% acetic acid) (80:20, v/v) with 0.6 mL/min at λ = 270 nm for phenol, methanol/water (containing 0.1% phosphoric acid) (55:45, v/v) with 1.0 mL/min at λ = 227 nm for BA, methanol/water (containing 1% acetic acid) (30: 70, v/v) with 0.8 mL/min at λ = 225 nm for CIP, acetonitrile/water (containing 1% oxalic acid) (20: 80, v/v) with 1.0 mL/min at λ = 365 nm for TC. Total organic carbon (TOC) removal efficiency of alloy-CA was assessed by a TOC analyzer (TOC-VCPN, Shimadzu, Japan). An electron paramagnetic resonance spectrometer (EPR, Bruker ESR5000) was employed to detect ROS during the reaction with the following settings: center field as 338 mT, sweep width as 50 mT, modulation as 0.2 mT and frequency as 100 kHz.

Supplementary Text 4. Steady-state concentration of ROS

The steady-state concentration of ROS ($[ROS]_{ss}$) was detected by analyzing the decay kinetics of probe chemicals. Benzoic acid (BA), nitrobenzene (NB) and furfuryl alcohol (FFA) were selected as the probes for $SO_4^{\bullet-}$, $HO^{\bullet}$ and $^1O_2$, respectively. The $[ROS]_{ss}$ can be expressed as:

$$\frac{d[probe]}{dt} = [ROS]_{ss} k_{ROS,probe} = k_{app,probe} \quad \text{(S1)}$$

$$[ROS]_{ss} = \frac{k_{app,probe}}{k_{ROS,probe}} \quad \text{(S2)}$$

where $k_{ROS,probe}$ represents the second-order rate constant for the degradation reaction between probe and ROS (Table S1). $k_{app,probe}$ is the pseudo-first-order rate constant for probe degradation.

Supplementary Tables

Supplementary Table 1. Content of metals in alloy-CA electrodes.

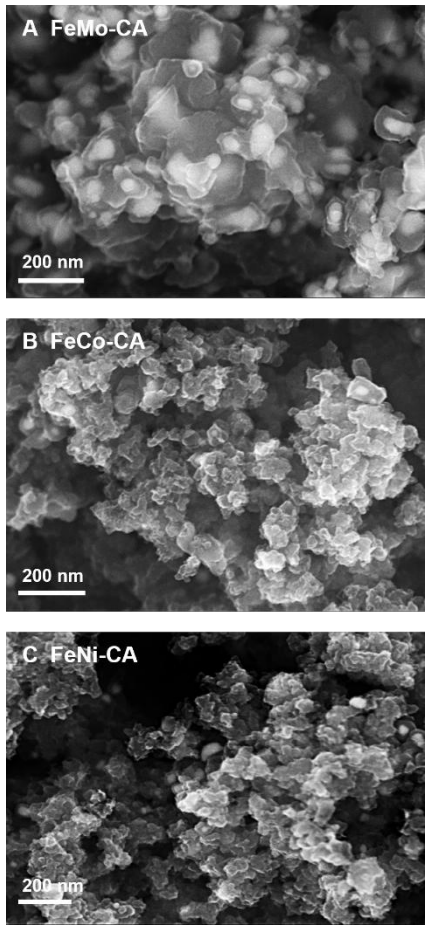
Content	Fe (wt.%)	Mo (wt.%)	Co (wt.%)	Ni (wt.%)
FeMo-CA	1.20	1.40	-	-
FeCo-CA	1.17	-	1.84	-
FeNi-CA	1.47	-	-	1.69

Supplementary Table 2. Second-order rate constants (k) of typical ROS for removing different probe chemicals.

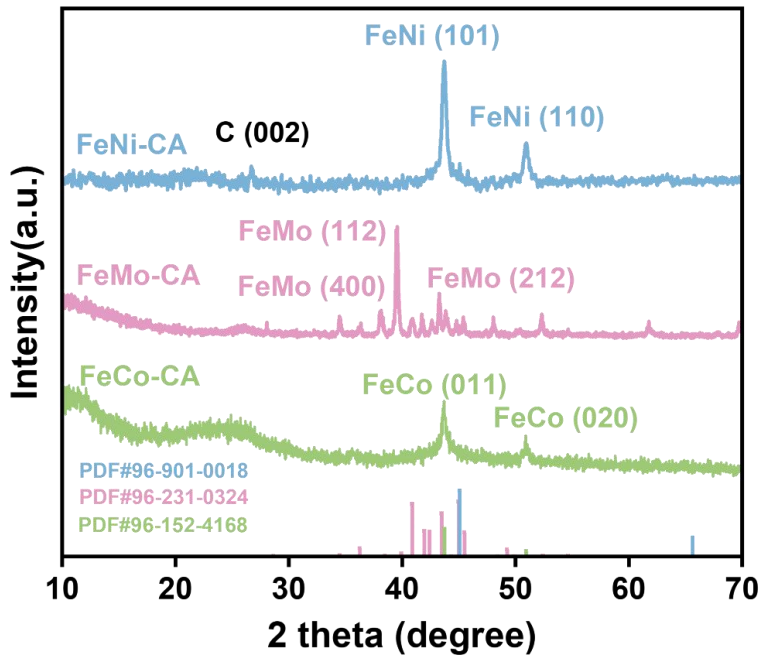
Pollutants	Second-order rate constants k ($M^{-1}s^{-1}$)		
	$SO_4^{\bullet-}$	$HO^{\bullet}$	$^1O_2$
Furfuryl alcohol (FFA)	n. a.[a]	1.5×10^{10}	1.2×10^8
Nitrobenzene (NB)	$\leq 10^6$	3.9×10^9	n. a.
Benzoic acid (BA)	1.2×10^9	4.3×10^9	n. a.

[a]not available

Supplementary Figures

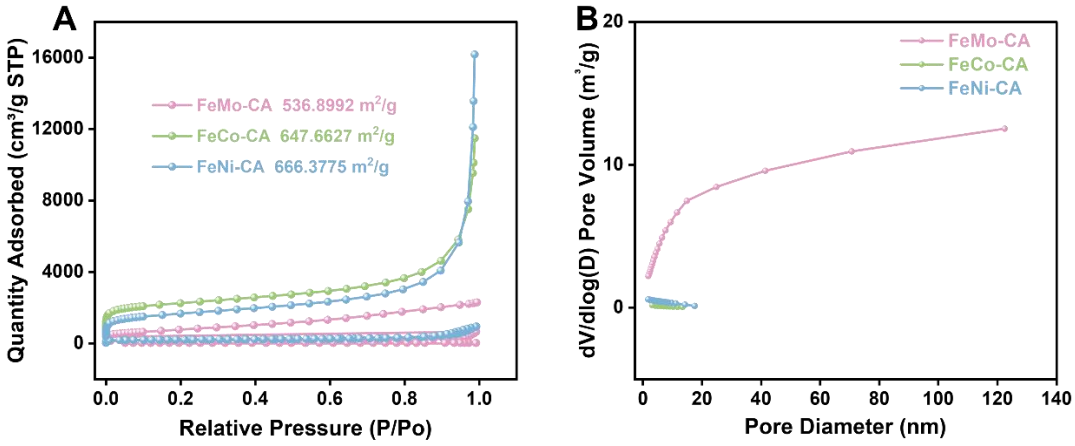


Supplementary Figure 1. SEM images of (A) FeMo-CA, (B) FeCo-CA and (C) FeNi-CA.



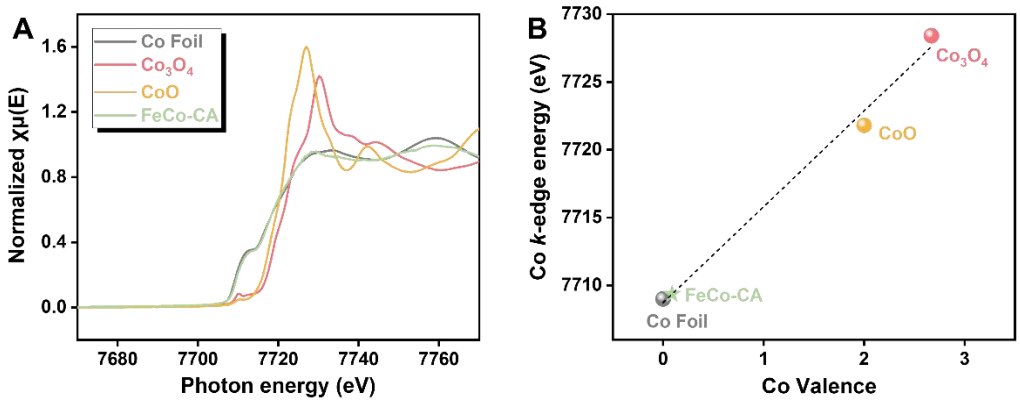
Supplementary Figure 2. XRD spectra of as-prepared alloy-CA electrodes.

The low-crystallinity carbon diffraction peaks of alloy-CA in XRD patterns originated from its intrinsically low graphitization degree, which was closely related to the sol–gel synthetic method of carbon aerogels. Specifically, the cross-linked phenolic resin three-dimensional network was formed by resorcinol and formaldehyde, which intrinsically lacked well-ordered graphitic sheet stacking. Only small carbon microcrystals with short-range order and long-range disorder structures were formed during carbonization. According to the Scherrer principle, small crystallite size and low stacking order of graphitic layers induced peak broadening and reduction in diffraction intensity. Therefore, the carbon diffraction peaks of alloy-CA were low-crystallinity.

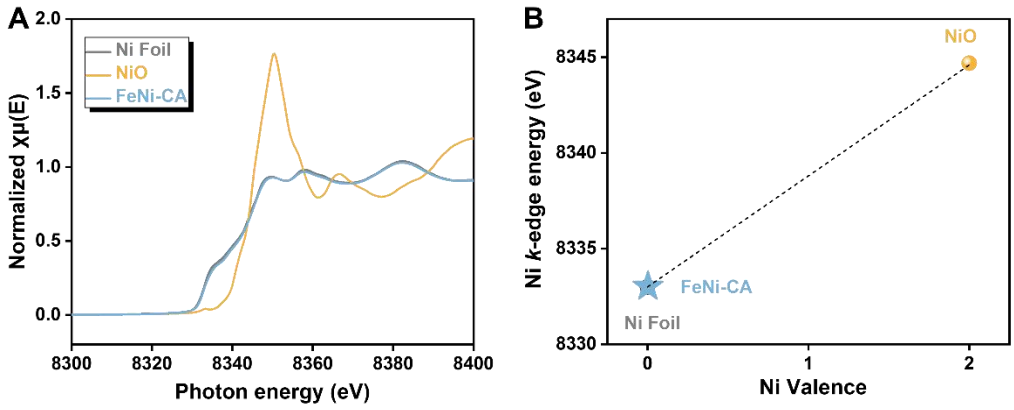


Supplementary Figure 3. (A) N_2 adsorption/desorption isotherms and (B) pore diameter distribution of FeMo-CA, FeCo-CA and FeNi-CA.

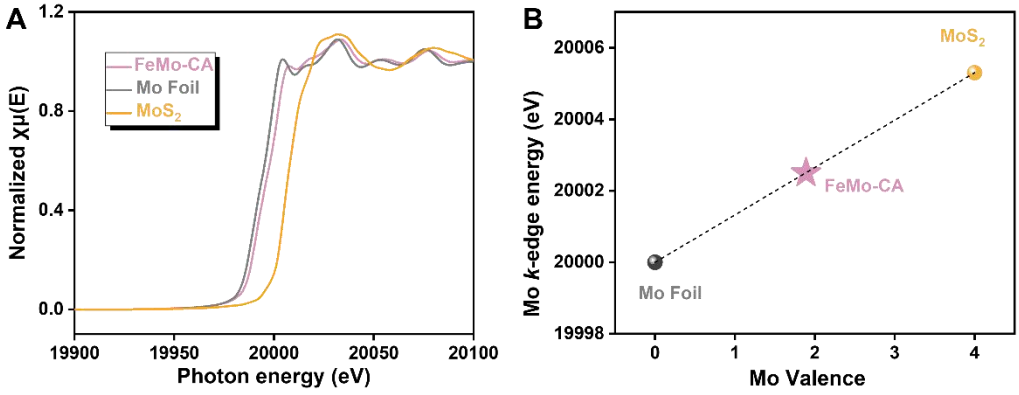
The pore size distribution (Supplementary Figure 3B) revealed that FeMo-CA possessed a much larger pore volume than FeCo-CA and FeNi-CA, with pore sizes spanning the mesopore-to-macropore range. In contrast, FeCo-CA and FeNi-CA showed limited pore volume.



Supplementary Figure 4. (A) Co K-edge XANES spectra and the corresponding (B) valence state for FeCo-CA.

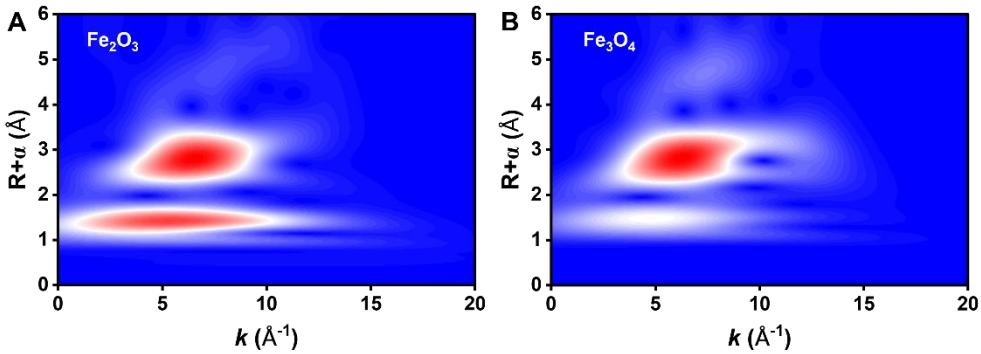


Supplementary Figure 5. (A) Ni K-edge XANES spectra and the corresponding (B) valence state for FeNi-CA.

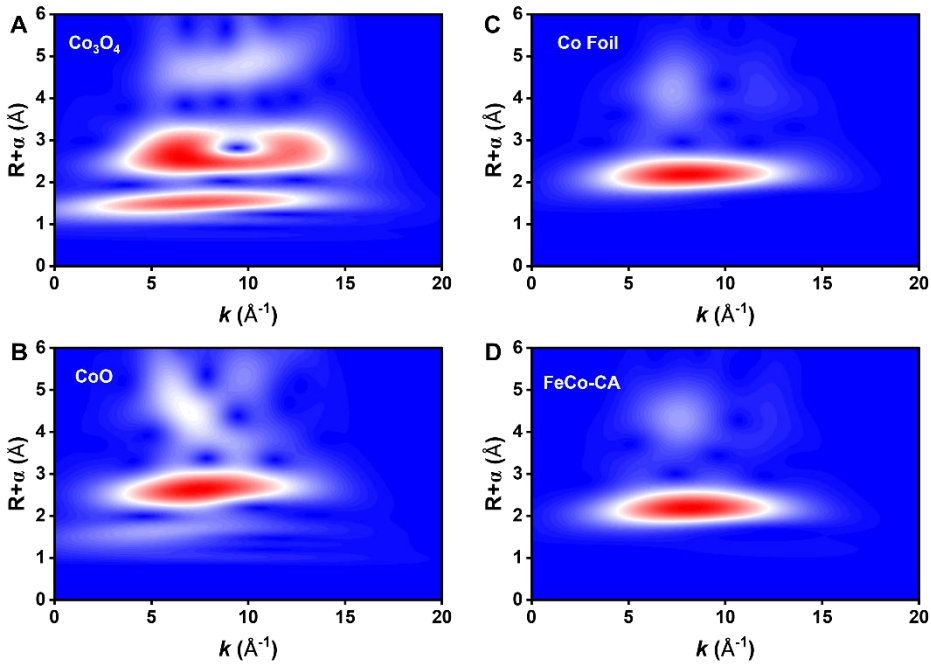


Supplementary Figure 6. (A) Mo K-edge XANES spectra and the corresponding (B) valence state for FeMo-CA.

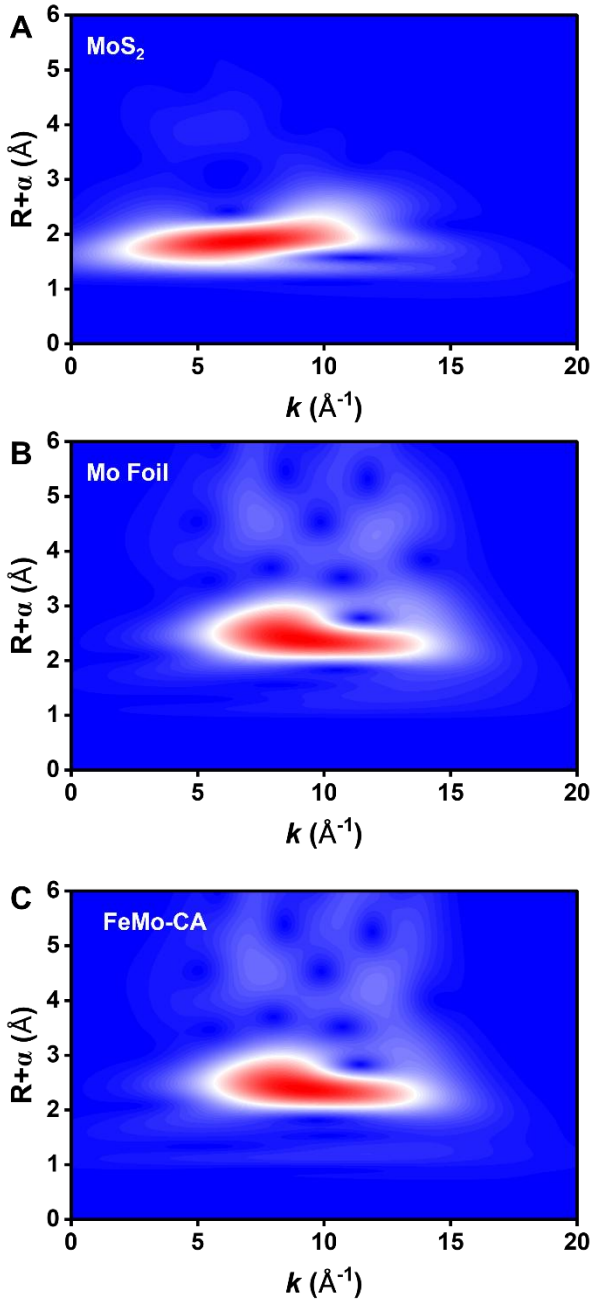
The distinctly positive valence of Mo (+1.89) compared with the zero valence of Fe, Co, and Ni was attributed to the intrinsic physicochemical properties of Mo. The carbon aerogel provided a reducing atmosphere during pyrolysis, which was sufficient to reduce Fe, Co, and Ni oxides to zero valence. However, the Mo-O bond was substantially stronger than the Fe-O, Co-O and Ni-O bonds, thereby making it difficult to reduce Mo^{6+} to Mo^0. Thus, Mo remained an intermediate oxidation state with an average valence of +1.89. Furthermore, the atomic radius of Mo was considerably larger than that of Fe, resulting in relatively poor Fe-Mo lattice matching. This structural mismatch hindered the complete incorporation of Mo into the Fe metallic lattice, which further resisted full reduction of Mo. In contrast, Fe, Co, and Ni possessed similar atomic radii and lattice structures, readily forming homogeneous solid solutions that could be fully reduced to the zero-valence state. Taken together, the +1.89 valence of Mo arose from the combined effects of Mo-O bond thermodynamic stability and lattice mismatch.



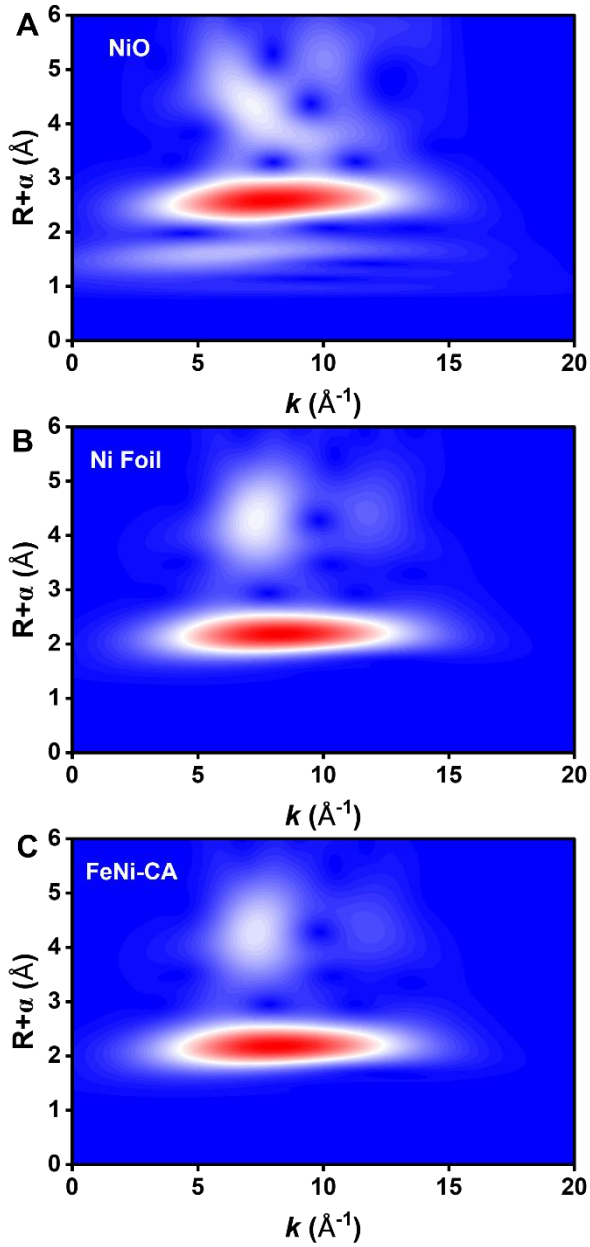
Supplementary Figure 7. WT-EXAFS of the Fe K-edge for (A) Fe_2O_3 and (B) Fe_3O_4, respectively.



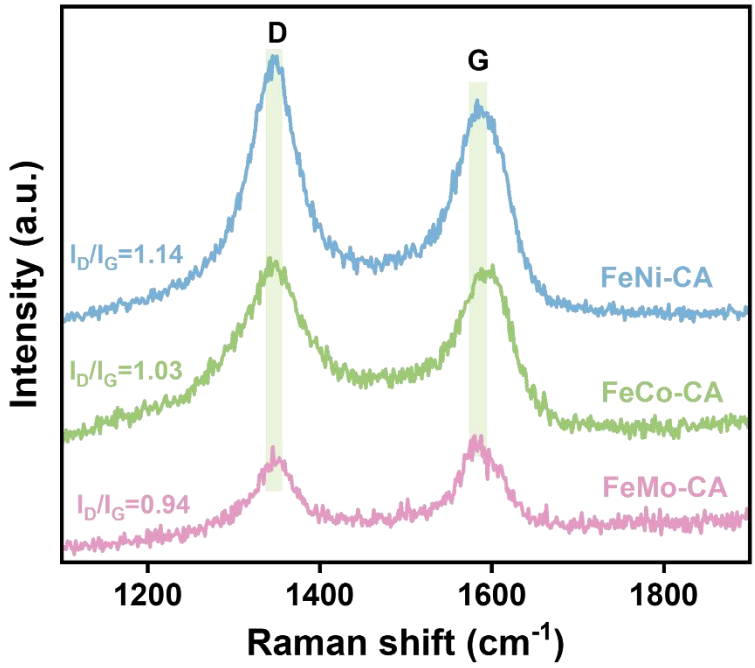
Supplementary Figure 8. WT-EXAFS of the Co K-edge for (A) Co_3O_4, (B) CoO, (C) Co foil and (D) FeCo-CA, respectively.



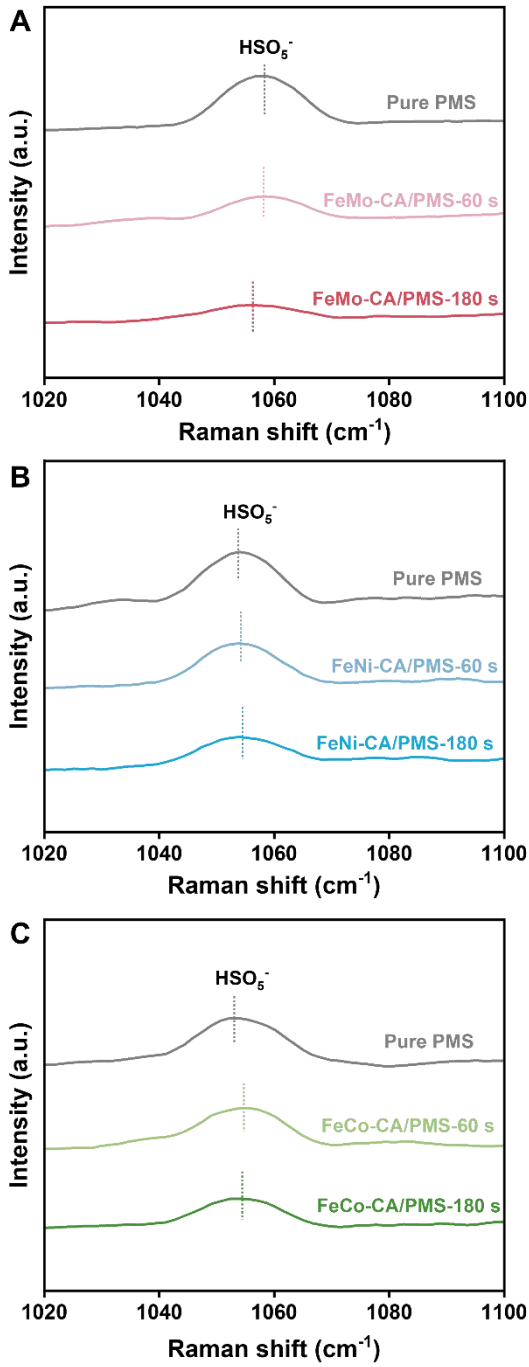
Supplementary Figure 9. WT-EXAFS of the Mo K-edge for (A) MoS_2, (B) Mo foil and (C) FeMo-CA, respectively.



Supplementary Figure 10. WT-EXAFS of the Ni K-edge for (A) NiO, (B) Ni foil and (C) FeNi-CA, respectively.



Supplementary Figure 11. Raman spectra of FeCo-CA, FeMo-CA and FeNi-CA.



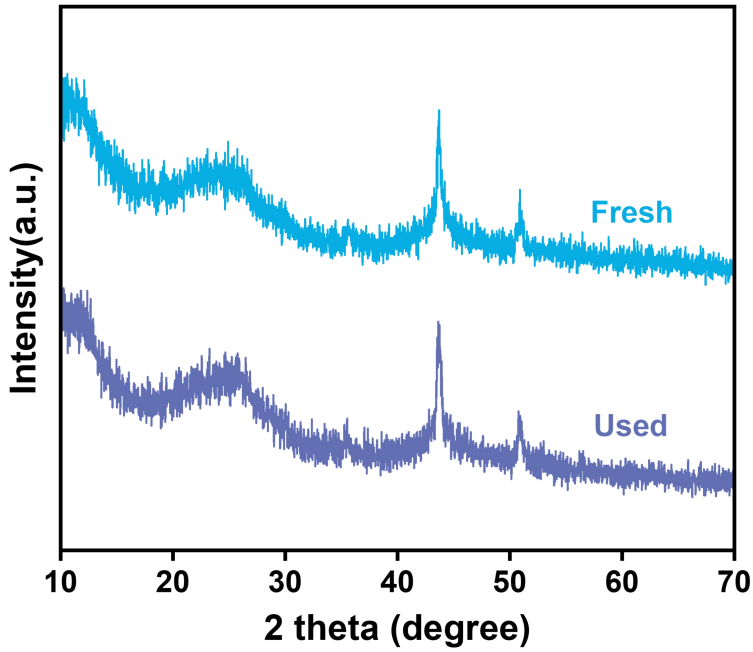
Supplementary Figure 12. *In situ* Raman spectra at the reaction times of 60 s and 180 s in (A) FeMo-CA/PMS, (B) FeNi-CA/PMS and (C) FeCo-CA/PMS systems.

The red/blue shift of the SO_3^- stretching band originates from the variation in bond order and bond length of the S-O bond in adsorbed PMS, which are directly governed by the direction of electron transfer between the alloy and PMS.

When the alloy center is electron-rich (e.g., FeMo-CA), electrons are transferred from the metal site into the antibonding orbitals of PMS, which reduces the S-O bond order, thereby lowering the vibrational frequency and producing a red shift of the SO_3^- peak. The effect lowers the O-O bond barrier, driving PMS decomposition via a radical pathway to generate $SO_4^{\bullet-}$.

In contrast, when the alloy center is electron-deficient (e.g., FeNi-CA), electrons from the bonding orbitals of PMS are drawn into empty metal orbitals. The reduced electron density increases the bond polarity of the S-O bond, giving rise to a higher vibrational frequency and a blue shift of the SO_3^- peak. PMS undergoes intramolecular rearrangement or terminal-oxygen adsorption, ultimately favoring $^1O_2$ generation via a non-radical pathway.

In a word, the shift direction of the SO_3^- stretching peak was used as a spectroscopic indicator for the direction of interfacial electron transfer.



Supplementary Figure 13. XRD patterns of the fresh and used FeCo-CA.